

## Increased oceanic dimethyl sulfide emissions in areas of sea ice retreat inferred from a Greenland ice core

Yutaka Kurosaki<sup>1,2</sup><sup>✉</sup>, Sumito Matoba<sup>2</sup><sup>✉</sup>, Yoshinori Iizuka<sup>2</sup><sup>2</sup>, Koji Fujita<sup>3</sup><sup>3</sup> & Rigen Shimada<sup>4</sup>

Ocean phytoplankton are an important source of dimethyl sulfide, which influences marine cloud formation. Model studies suggest that declines in Arctic sea ice may lead to increased dimethyl sulfide emissions, however observational support is lacking. Here, we present a 55-year high-resolution ice core record of methane sulfonic acid flux, an oxidation product of dimethyl sulfide, from the southeast Greenland Ice Sheet. We infer temporal variations in ocean dimethyl sulfide emissions and find that springtime (April–June) fluxes of methane sulfonic acid correlate well with satellite-derived chlorophyll-*a* concentration in the Irminger Sea. Summertime (July–September) methane sulfonic acid fluxes were 3 to 6 times higher between 2002–2014 than 1972–2001. We attribute this to sea ice retreat day becoming earlier and a coincident increase in chlorophyll-*a* concentration in the adjacent open coastal waters.

<sup>1</sup>Graduate School of Environmental Science, Hokkaido University, Sapporo, Japan. <sup>2</sup>Institute of Low Temperature Science, Hokkaido University, Sapporo, Japan. <sup>3</sup>Graduate School of Environmental Studies, Nagoya University, Nagoya, Japan. <sup>4</sup>Earth Observation Research Center, Japan Aerospace Exploration Agency, Tsukuba, Japan. ✉email: [kurosaki\\_yutaka@frontier.hokudai.ac.jp](mailto:kurosaki_yutaka@frontier.hokudai.ac.jp); [matoba@lowtem.hokudai.ac.jp](mailto:matoba@lowtem.hokudai.ac.jp)

Dimethyl sulfide (DMS), which originates from ocean phytoplankton, is oxidized to non-sea-salt sulfate ( $\text{nssSO}_4^{2-}$ ) and methane sulfonic acid (MSA) after emission into the atmosphere<sup>1</sup>. These aerosols contribute to the formation of cloud condensation nuclei in the marine atmosphere and participate in cloud radiative forcing and direct aerosol radiative forcing<sup>2,3</sup>. As the oceanic flux of DMS accounts for 10–40% of the total global sulfur flux<sup>4</sup> and impacts the formation of cloud condensation nuclei in the marine atmosphere, DMS is an important factor used to calculate the radiative forcing from the climate model<sup>5,6</sup>.

DMS emissions from the ocean to the atmosphere are determined by the gas transfer coefficient from the ocean to the atmosphere, the solubility of gaseous DMS, and the DMS concentrations in water and air<sup>7,8</sup>. The gas transfer coefficient shows a linear dependence on mean horizontal wind speed to  $11 \text{ m s}^{-1}$ , but the relationship between the gas transfer coefficients and wind speed weakens at higher wind speeds<sup>9,10</sup>. The DMS in the ocean is converted from dimethylsulfoniopropionate (DMSP), a product of phytoplankton, by the enzyme system of bacteria<sup>1</sup>. Therefore, the concentration of DMS in the ocean is estimated from the chlorophyll-a (Chl-a) concentration. Gali et al.<sup>11</sup> estimated the DMS concentration at the sea surface at global and regional scales with a new remote sensing algorithm using remotely sensed Chl-a along with light penetration and climatological mixed-layer depth. The estimation of the DMS concentration at the sea surface by the new algorithm was improved at the global scale, but the estimation disagreed with the regional scale and seasonal variation. Gali et al.<sup>12</sup> noted that the shortcomings of the new algorithm were due to sparse and biased in situ DMS data.

Arctic temperatures are rising twice as fast as the global average, and the summer seasonal sea ice extent has declined sharply in recent decades<sup>13,14</sup>. In the Arctic region, the decline in seasonal sea ice cover increases the light penetration on the surface and subsurface of the ocean and promotes the primary production of phytoplankton<sup>12,14–17</sup>. In the satellite and model-based estimation, the DMS emissions increased in the last decade because of the decline in the seasonal sea ice cover in the pan-Arctic<sup>12,17</sup>. However, there is little observational evidence for the recent increase in DMS emission in the pan-Arctic. To estimate the changes of the impact of DMS emission on the global climate, long-term and continuous aerosol monitorings are needed.

When DMS is released from the ocean to the atmosphere, DMS is oxidized to MSA and non-sea-salt sulfate. The MSA in aerosols is used as an indicator of oceanic DMS emission because the natural origin of MSA is almost exclusively limited to the oxidation of DMS. Sharma et al.<sup>18</sup> showed that aerosol MSA concentrations at three stations in the Arctic (Alert-Nunavut, Barrow-Alaska, and Ny-Ålesund-Svalbard) increased since 2000 with respect to 1990, and suggested that the increase in MSA resulted from the northward migration of the marginal ice edge zone. Except for the 3 stations, there are no long-term continuous monitoring data for aerosol MSA in the pan-Arctic region<sup>19</sup>. Ice cores drilled from ice sheets and glaciers are useful archives for reconstructing past aerosol history<sup>20,21</sup>. Aerosol MSA is preserved in ice sheets and glaciers after wet or dry deposition from the atmosphere to the snow surface<sup>22</sup>, but the MSA in the snowpack at low accumulation areas is released from the snow surface to the atmosphere, called postdepositional loss<sup>23,24</sup>. Therefore, drilling sites must be selected at high accumulation and cold areas of ice sheets and glaciers.

The southeastern dome of the Greenland Ice Sheet (SE-Dome;  $67.18^\circ\text{N}$ ,  $36.37^\circ\text{W}$ , 3170 m above sea level, Fig. 1) has the distinct characteristic of having a high accumulation rate ( $1.01 \pm 0.22 \text{ m water equivalent yr}^{-1}$ ) and low annual mean temperature

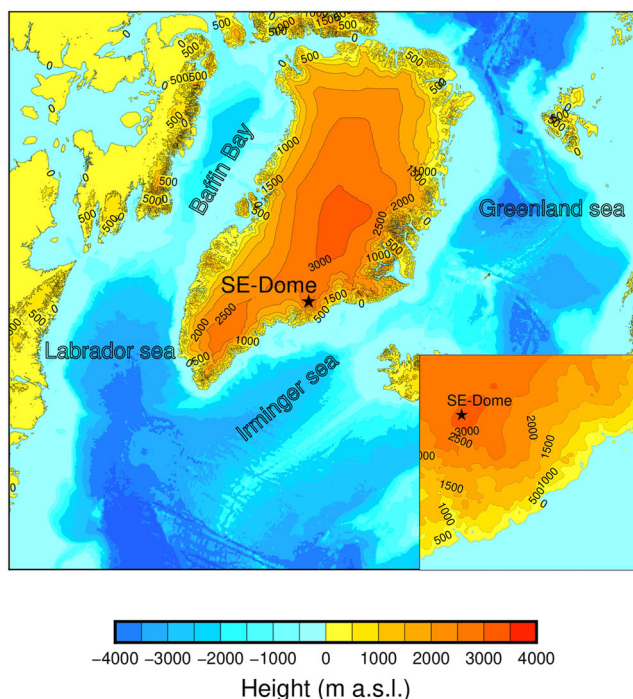


**Fig. 1 SE-Dome site.** The black star shows the location of the SE-Dome site. The color shade denotes topography provided by ETOPO1, which is a 1 arc-minute global relief model of Earth's surface that integrates land topography and ocean bathymetry. The height of Greenland denotes the top of the Ice Sheet.

( $-20.9^\circ\text{C}$ )<sup>21,25,26</sup>. The accumulation rate is the highest among the domes on the polar ice sheets, at 3–4 times that of typical domes of Greenland Ice Sheet<sup>25,26</sup>. Therefore, even nitrate, which is a volatile species, was preserved in the SE-Dome ice core without any effects of postdepositional loss<sup>21</sup>, the dating of the SE-Dome ice core was determined by a comparison of  $\delta^{18}\text{O}$  records from the ice core and a record simulated by isotope-enabled climate models with an accuracy of 1 month in most period<sup>26</sup> (Method). Consequently, the ice core obtained from the SE-Dome allows us to reconstruct the seasonal variations in MSA from 1960 to 2014<sup>21,26</sup>. The objective of this study is to reveal the temporal variations in DMS emissions from the ocean to the atmosphere around the seasonal sea ice region using the high-time-resolution MSA profile in the SE-Dome ice core.

## Results and discussion

**Decadal and seasonal variation in the MSA flux.** The mean annual flux of MSA ( $\text{MSA}_{\text{flux}}$ ) (Method) from 2002–2014 was substantially higher than that from the complete study period (1960–2014) (Fig. 2a and Table 1). On the other hand, the mean of annual  $\text{MSA}_{\text{flux}}$  from 1972–2001 was substantially lower than the mean of the entire period (Table 1). The interannual trend of annual  $\text{MSA}_{\text{flux}}$  substantially decreased from 1960 to 2001 ( $-0.0061 \text{ mg m}^{-2} \text{ yr}^{-1}$ ,  $p < 0.05$ ). The decrease trend in the  $\text{MSA}_{\text{flux}}$  in the SE-Dome ice core from 1960–2001 is consistent with the variations in MSA concentration in ice cores from the inland Greenland Ice Sheet, which showed declining trends over the late nineteenth and twentieth centuries<sup>27–29</sup>. However, the increase in the  $\text{MSA}_{\text{flux}}$  in the SE-Dome ice core after 2002 has not been found in other ice cores. We divided the entire period into three periods (1960–1971, 1972–2001, and 2002–2014) to investigate the behavior of MSA for the following discussion.

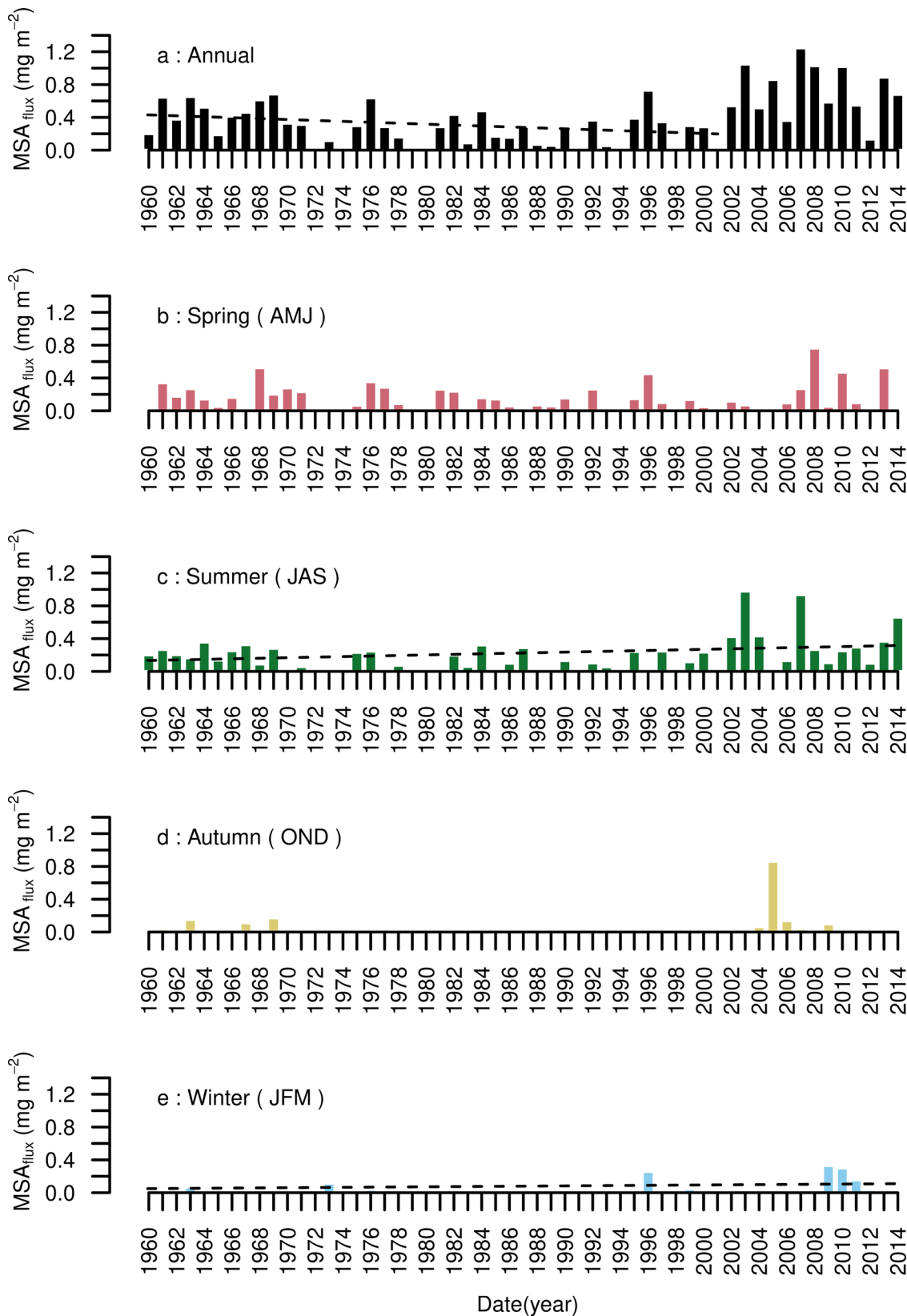


**Fig. 2 Interannual variations in MSA<sub>flux</sub>.** a-e denote the interannual variations in MSA<sub>flux</sub> of annual and each season (a: January–December, b: January–March, c: April–June, d: July–September, e: October–December). Black dashed lines are regression lines.

**Table 1 Mean annual MSA<sub>flux</sub> for each period and their differences from the entire period.**

Period	Mean $\pm \sigma$ ( $\text{mg m}^{-2} \text{yr}^{-1}$ )	Difference ( $\text{mg m}^{-2} \text{yr}^{-1}$ )	<i>p</i> -value
1960–2014	0.39 $\pm$ 0.31	–	–
1960–1971	0.45 $\pm$ 0.18	0.06	0.23
1972–2001	0.21 $\pm$ 0.20	–0.18	<0.01
2002–2014	0.73 $\pm$ 0.32	0.34	<0.01

$\sigma$  is the standard deviation of MSA<sub>flux</sub> for each period. *p*-value is significance of the differences by Student's *t*-test.

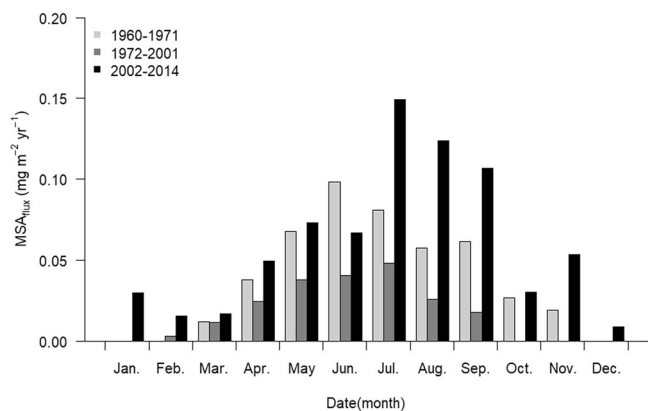


**Fig. 3 Monthly MSA<sub>flux</sub>.** The bar graphs colored by light gray, dark gray, and black denote the monthly MSA<sub>flux</sub> from 1960–1971, 1972–2001, and 2002–2014, respectively. The MSA<sub>flux</sub> is the mean value for each period in a month. We defined January–March, April–June, July–September, and October–December as winter, spring, summer, and autumn, respectively.

The mean MSA<sub>flux</sub> from 1960–1971 increased from March, peaked in June, and gradually decreased toward November (Fig. 3, light gray). The mean MSA<sub>flux</sub> from 1972–2001 increased from February, peaked in July, and rapidly decreased toward September (Fig. 3, dark gray). The mean MSA<sub>flux</sub> from 2002–2014 existed throughout the year, increased from March, peaked in July, and maintained high values until September (Fig. 3, black). The July to September MSA<sub>flux</sub> from 2002–2014 was 3–6 times higher than that from 1972–2001 (Fig. 3). In the northern part of the North Atlantic, phytoplankton blooms start during April–June offshore of the north of 45°N and during July–August in the seasonal sea ice area on the southeastern coast of Greenland<sup>30</sup>. Based on the seasonal variation in the MSA<sub>flux</sub> and the phytoplankton bloom, we defined April–June as “spring”, July–September as “summer”, October–December as “autumn”, and January–March as “winter”.

Most MSA (76%) is deposited on the snow surface by wet deposition<sup>31</sup>. Therefore, a high annual snow accumulation results in a high amount of MSA deposition. The reconstructed seasonal accumulation rate showed no seasonal difference (spring: 0.25  $\pm$  0.07 m, summer: 0.25  $\pm$  0.09 m, autumn: 0.27  $\pm$  0.09 m and winter: 0.25  $\pm$  0.07 m)<sup>26</sup>. Moreover, the accumulation rates in spring and summer did not change from 1960 to 2014<sup>26</sup>. Consequently, we suggest that the recent increase in summer MSA<sub>flux</sub> was caused by the increase in MSA concentration in the atmosphere from the changes in the seasonality of phytoplankton blooms and/or DMS emissions in the northern part of the North Atlantic, and not by the changes in precipitation seasonality. Next, we discuss the process of the MSA<sub>flux</sub> variation in the spring (April–June), summer (July–September), autumn (October–December), and winter (January–March).

**Spring MSA flux.** The spring MSA<sub>flux</sub> did not substantially change from 1960–2014 (+0.0002  $\text{mg m}^{-2} \text{yr}^{-1}$ ,  $p = 0.8888$ ) (Fig. 2b). Important factors controlling DMS emissions from the ocean to the atmosphere include the DMS concentration at the ocean surface and wind stress on the ocean<sup>7,8</sup>. High concentrations of DMS at the ocean surface enhance the emission of DMS from the ocean to the atmosphere<sup>8,32</sup>. The gas transfer coefficient for DMS emission exhibits the highest values at intermediate wind speeds (8–11  $\text{m s}^{-1}$ )<sup>9,10</sup>. We investigated the contributions of these factors to the variation in MSA<sub>flux</sub> in the SE-Dome ice core described below. The correlation coefficient between the aerial average of Chl-a (Methods) in the Irminger Sea (55°N–62°N, 22°W–38°W, dashed line box in Fig. 4a, c) and spring MSA<sub>flux</sub> was 0.69 ( $p < 0.01$ ) (Fig. 4a, b). On the other hand, the spring MSA<sub>flux</sub> did not correlate with the frequency of intermediate wind (Methods) in the Irminger Sea ( $r = 0.04$ ,  $p = 0.87$ ) (Fig. 4c, d). A backward trajectory analysis (Methods) showed that transportation of air masses from the possible source region of MSA to the SE-Dome has been unchanged (Supplementary Fig. 1). Consequently, the spring MSA<sub>flux</sub> in the SE-Dome ice core was dominated by the Chl-a concentration in the Irminger Sea.

**Summer MSA flux.** The summer MSA<sub>flux</sub> substantially increased from 1960 to 2014 (+0.0037  $\text{mg m}^{-2} \text{yr}^{-1}$ ,  $p < 0.05$ ) (Fig. 2c). Moreover, the summer MSA<sub>flux</sub> from 2002–2014 was 3–6 times higher than that from 1972–2001 (Fig. 3). The spatial distribution of air mass transportation was stable for the entire period (Supplementary Fig. 2). We can assume that the recent high values of summer MSA<sub>flux</sub> were not caused by changing transportation processes but by changes in phytoplankton production, sea ice conditions, and wind stress along the southeastern coast of Greenland. However, distribution maps of the correlation coefficient between the summer MSA<sub>flux</sub> and Chl-a concentration, frequency of intermediate wind, and sea ice concentration show that these indices did not correlate with the summer MSA<sub>flux</sub> (Supplementary Fig. 3). Although the spring MSA<sub>flux</sub> was quantitatively correlated with the Chl-a concentration in the Irminger Sea (Fig. 4a, b), the summer MSA<sub>flux</sub> did not correlate with any factors.

We focused on a sea ice retreat day for each period (1960–1971, 1972–2001, 2002–2014) (Fig. 5) and the ratio of open water extent for spring to summer (Supplementary Fig. 4) in the cumulative density function 40 % region (CDF40) of air mass probability revealed by the backward trajectory analysis during summer from 1960–2014 (Method). While almost all sea ice on the southeastern coast of Greenland disappeared during July (182–212 days of year (DOY)) from 2002–2014, the sea ice remained even in August (213–243 DOY) from 1972–2001 and in September (244–273 DOY) from 1960–1971 (Fig. 5). The ratio of the open water extent in the CDF40 region increased from 1960 to 2014 in every month, and the sea ice in the CDF40 region has disappeared completely during July since 2002 (Supplementary Fig. 4). The Chl-a concentration in the CDF40 region from 2002–2014 was substantially higher than that from 1998–2001 (Supplementary Fig. 5a). On the other hand, the frequency of intermediate wind in the CDF40 region from 2002–2014 was not substantially differ that from 1998–2001 (Supplementary Fig. 5b). The appearance frequency of higher Chl-a concentrations in CDF40 region has clearly increased in the 2002–2014 (Fig. 6). Therefore, we conclude that the summer DMS emissions due to the high production of phytoplankton have been enhanced and thus preserved as MSA in the SE-Dome ice core.

We can speculate why the summer MSA<sub>flux</sub> from 2002–2014 increased 3–6 times compared to that from 1972–2001 as follows.

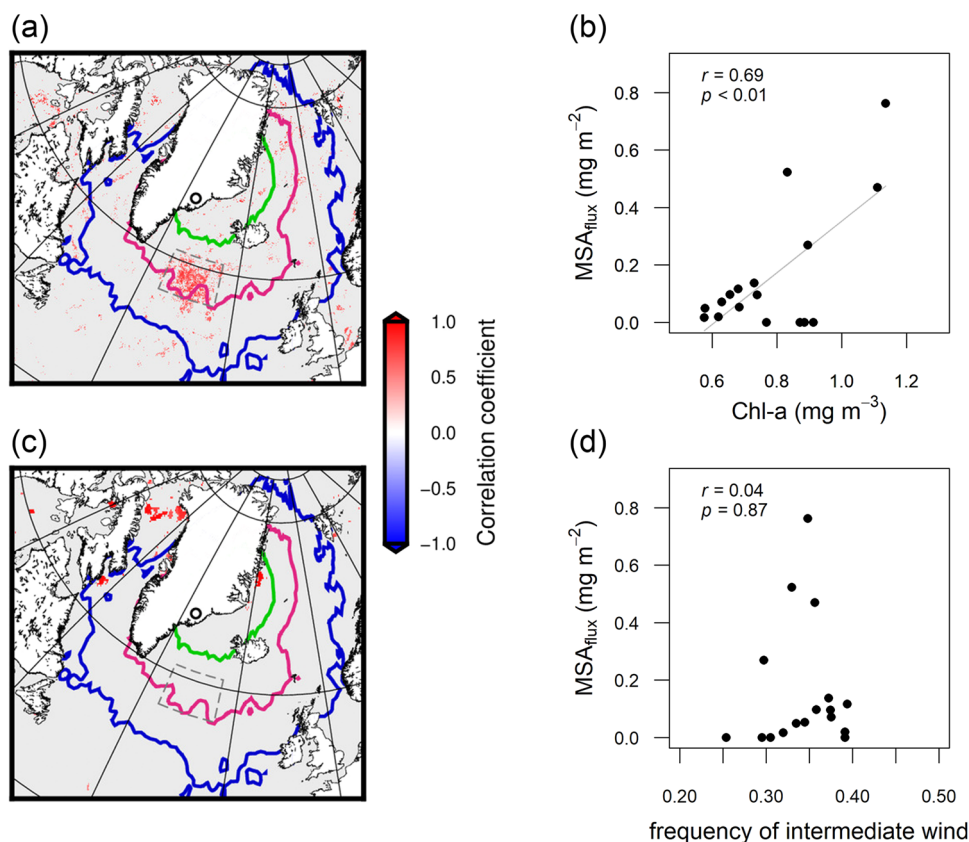


**Fig. 4 The relationship between the spring MSA<sub>flux</sub> and each factor.** **a** Correlation coefficient between MSA<sub>flux</sub> and Chl-a during spring from 1998–2014. **b** Scatter plot of MSA<sub>flux</sub> and Chl-a during spring. **c** Correlation coefficient between MSA<sub>flux</sub> and the frequency of intermediate wind during spring from 1998–2014. **d** Scatter plot of MSA<sub>flux</sub> and frequency of intermediate wind during spring. Colored regions in **a** and **c** denote  $p < 0.05$  with Student’s *t*-test. Green, purple, and blue contours in **a** and **c** denote the cumulative density function 40%, 60%, and 80% region, respectively, of air mass probability revealed by the backward trajectory analysis during spring from 1960–2014 (Method). Gray dashed boxes in **a** and **c** denoted the area of 55°N–62°N and 22°W–38°W. The values of the Chl-a in **b** and the frequency of intermediate wind in **d** are the spatial means in gray dashed boxes in **a** and **c**. Black circles in **a** and **c** show the position of the SE-Dome site. Gray line in **b** is the regression line.

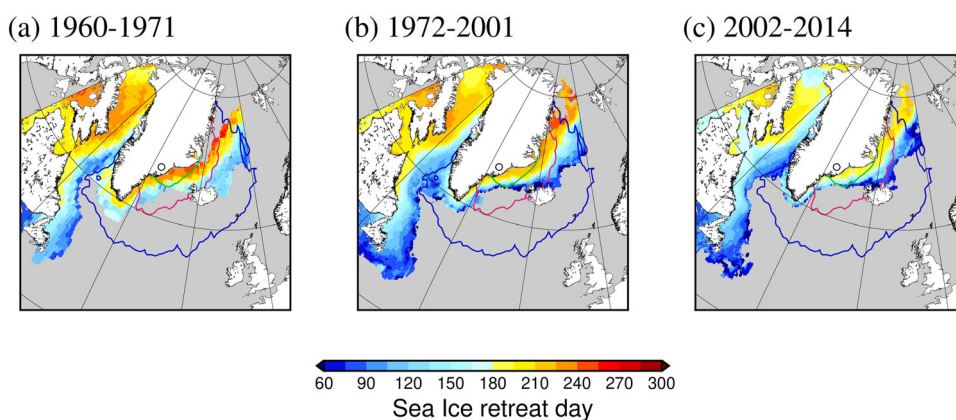


**Fig. 5 Sea ice retreat day.** **a–c** denote the sea ice retreat day of the year around Greenland (40°N–85°N, 0°W–80°W) for each period. Green, purple, and blue contours denote the regions greater than 40%, 60%, and 80% in the cumulative density function, respectively, of air mass probability revealed by the backward trajectory analysis during summer from 1960–2014. Black circles are the position of the SE-Dome site.

Sea ice retreat occurred in CDF40 during July from 2002–2014. Remarkably, this is ~1 month earlier than from 1972–2001. The climatology of sea surface photosynthetically active radiation over the region of 60°N peaks in July<sup>17</sup>. The earliness of sea ice retreat and the increase in Chl-a concentration in CDF40 occurred from 2002–2014 simultaneously (Fig. 5 and Supplementary Fig. 5a).

The lack of sea ice during July increases the light penetration at the surface and subsurface, and then enhances the production of phytoplankton and lengthens the bloom period. The summer MSA<sub>flux</sub> in the ice core results from the early retreat of the sea ice in CDF40 followed by an increase in DMS emissions from enhanced phytoplankton production.

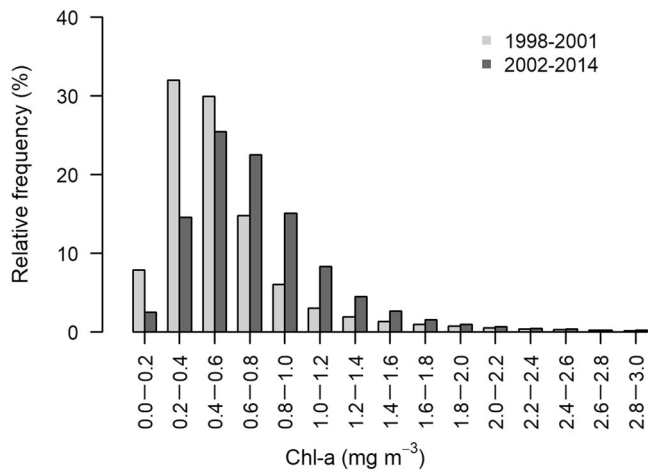


**Fig. 6 Relative frequency of Chl-a concentrations.** Light gray and dark gray bar graphs denote the relative frequency of the Chl-a concentrations from 1998–2001 and 2002–2014, respectively. This is the ratio from all grid cells with sea ice concentrations below 10% within the region of CDF40 during summer from 1960–2014.

**Autumn MSA flux.** MSA<sub>flux</sub> during autumn (from October to December) was more detected from 2002–2014 (Figs. 2d and 3). The autumn accumulation rate in SE-Dome ice core also substantially increased from 1960 to 2014<sup>26</sup>. As the increase in precipitation causes the increase of wet deposition of atmospheric substances, the increase in autumn precipitation may be one of the reasons for the increase in autumn MSA<sub>flux</sub>. However, we cannot ignore the possibility of the occurrences of the autumn bloom of phytoplankton in the pan-Arctic region<sup>33</sup> as the reason for the increase in autumn MSA<sub>flux</sub>. The frequency of autumn blooms of phytoplankton increased in the pan-Arctic because the increase in storm days at the ocean before sea ice cover enhanced vertical mixing, conveying the nutrients from the deeper waters to the sea surface<sup>33</sup>.

**Winter MSA flux.** MSA<sub>flux</sub> during winter (from January to March) substantially increased from 1960–2014 ( $+0.0012 \text{ mg m}^{-2} \text{ yr}^{-1}$ ,  $p < 0.05$ ) (Figs. 2e and 3). The MSA<sub>flux</sub> in January was only detected from 2002–2014 (Fig. 3). Commonly, phytoplankton growth in mid- and high-latitude ocean in winter is limited because of deep mixing layer and low solar radiation. However, recently widespread winter phytoplankton blooms were observed in a large part of the North Atlantic sub-polar gyre triggered by intermittent restratification of the mixed layer when mixed-layer eddies led to a horizontal transport of lighter water over denser layers<sup>34</sup>. We speculate that the recent increase in MSA<sub>flux</sub> during winter could result from the recent observed phytoplankton bloom in winter in the North Atlantic.

**Implication.** The results of SE-Dome ice core analysis showed the 3–6 times increase in summer MSA<sub>flux</sub> since 2002. We suggested that the reason for the increase in summer MSA<sub>flux</sub> was the early sea ice retreat followed by an increase in DMS emissions from enhanced phytoplankton production. The similar early retreat of sea ice and the increase in Chl-a concentration also observed in offshore of Ilulissat in Baffin Bay after 2002 (Fig. 5 and Supplementary Fig. 5). Additionally, process-based studies indicated that the accelerated decline of the sea ice in the pan-Arctic region since the 2000s could be associated with upward trends in oceanic DMS flux in the pan-Arctic<sup>12,17</sup>. Therefore, the increase in oceanic DMS emission in summer, which was the new observational truth by the SE-Dome ice core, could already occur in other

seasonal sea ice areas. Under the future climate warming, we expect that the ocean areas increasing in the summer DMS emission were expanded. This suggests that negative cloud radiative forcing may be enhanced and mitigate the positive ice-albedo feedback in the pan-Arctic because of increasing low clouds in the marine atmosphere. Although the spring bloom has been pointed as the most dominant factor for the oceanic natural sulfur emission until now, our study suggests that the process of the summer DMS emission and the direct and indirect effect of the radiation balance in accordance with the summer DMS emission would be more important for the estimation of the future radiation balance.

## Conclusions

We reconstructed the annual and seasonal MSA<sub>flux</sub> from 1960 to 2014 with monthly resolution from a high-resolution ice core obtained from the SE-Dome, southeastern Greenland Ice Sheet. The annual MSA<sub>flux</sub> decreased from 1960 to 2001 and markedly increased after 2002 (Fig. 2). We investigated the most dominant factor for the recent increase in the annual MSA<sub>flux</sub> by defining April–June as “spring”, July–September as “summer” October–December as “autumn”, and January–March as “winter”.

The spring MSA<sub>flux</sub> was significantly correlated with the Chl-a concentration in the Irminger Sea ( $r = 0.69$ ,  $p < 0.01$ ) (Fig. 4). The summer MSA<sub>flux</sub> from 2002–2014 was 3–6 times higher than that from 1972–2001 (Fig. 3). This was the most dominant reason for the increase of annual MSA<sub>flux</sub> from 2002. We suggested that the reason for the increased summer MSA<sub>flux</sub> was the early sea ice retreat followed by the increase in oceanic DMS flux from the increase in phytoplankton production at the ocean surface and subsurface. The autumn MSA<sub>flux</sub> was more detected from 2002–2014 (Figs. 2d and 3). The winter MSA<sub>flux</sub> substantially increased from 1960 to 2014 (Figs. 2e and 3). The winter MSA in the SE-Dome ice core could be sourced by the winter phytoplankton bloom in the North Atlantic sub-polar gyre.

This ice core study concludes that ocean phytoplankton productivity and oceanic DMS emissions have increased since the early 2000s in seasonal sea ice areas. Data suggest that such increase in the oceanic DMS emissions could already occur in other regions where the early retreat of seasonal sea ice occurs. This suggests that negative cloud radiative forcing may be enhanced because of increasing low clouds in the marine atmosphere.

## Methods

**Dating of the SE-Dome ice core.** The SE-Dome ice core was dated based on pattern matching of the  $\delta^{18}\text{O}$  variations between the ice core record and a simulated profile in Furukawa et al.<sup>26</sup>. The simulated profile of  $\delta^{18}\text{O}$  ( $\delta^{18}\text{O}_{\text{model}}$ ) was constructed by a regional climate model with isotope diagnostics included in the hydrological cycle (REMO-iso)<sup>35</sup> and an atmospheric general circulation model (GCM), into which stable water isotopes are incorporated (iso-GSM)<sup>36</sup>. The SE-Dome  $\delta^{18}\text{O}$  and  $\delta^{18}\text{O}_{\text{model}}$  variations were matched by selecting manually 170 tie points from 0.8 to 86.5 m depth using AnalySeries software<sup>37</sup>. This matching provides a relationship between the depth (ice core) and date (model). Then, the SE-Dome core age scale based on the isotope composition was constructed by linearly interpolating between the points. To obtain the annual accumulation rate, the depth was resampled at 1-year intervals based on the age scale. The depth of a 1-year interval indicates the annual accumulation rate in snow equivalents. Then, the snow accumulation rate in water equivalent depth was calculated by multiplying snow density. In the same way, the seasonal accumulation rates were obtained based on seasonal boundaries of 1 March, 1 June, 1 September, and 1 December. The varying uncertainty from section to section was calculated by using an algorithm<sup>38</sup> based on a Monte Carlo simulation fitting ensembles of straight lines to subsets of the age data. An age determination error at each tie point should be assigned to calculate a confidence limit. We assumed that the error at each tie point is  $\pm 1$  month because most of the interannual  $\delta^{18}\text{O}_{\text{model}}$  peaks, selected for tie points, consisted of three data points. In most periods, the 95% confidence limit was around 1 month (average  $\pm 0.9$  months). However, there were larger

uncertainties where the number of tie points was small. The largest uncertainty was found in October 2004 ( $\pm 2.4$  months).

**MSA analysis and processing in the SE-Dome ice core.** We analyzed a 90.45 m depth ice core drilled at the SE-Dome site<sup>39</sup>. For analyses of chemical species in the ice core, we divided the ice core into 100 mm depth sections in a cold room. The samples were decontaminated using a clean ceramic knife in a cold clean room (class 10,000), put into a cleaned polyethylene bottle, and then melted in the bottle at room temperature in a clean room. The methane-sulfonate ion (MS<sup>-</sup>) was measured by ion chromatography (Thermo Scientific, ICS-2100). We used a Dionex AS-14A column with 23 mM KOH gradient eluent for MS<sup>-</sup> (we describe MS<sup>-</sup> as MSA). The injection volume of the sample was 1 mL. The number of samples was 395 from 1960 to 2014, corresponding to  $\sim 7$  samples per year on average. Annual and seasonal fluxes of MSA (MSA<sub>flux</sub>) were calculated by multiplying an MSA concentration by a water equivalent value of the vertical thickness of the sample for each season (annual: January–December, winter: January–March, spring: April–June, summer: July–September, autumn: October–December).

**Uncertainty due to the ice core dating.** We evaluated the uncertainty of interannual and seasonal variations in MSA<sub>flux</sub> resulting from the age determination error in the SE-Dome ice core. The age determination error of each sample was assigned a random number based on a standard normal distribution, which was derived from the 95 % confidence limit of the age of each sample in Furukawa et al.<sup>26</sup>. The age of each sample was re-assigned from the age determination error. We re-calculated the interannual and seasonal variations in MSA<sub>flux</sub> using the re-assigned age scale. We repeated this processes in 1000 times and obtained 1000 different interannual and seasonal variations in MSA<sub>flux</sub> to eliminate the bias based on the random number generation. We calculated mean values and standard deviations with these 1000 profiles of MSA<sub>flux</sub>. As the result, the interannual and seasonal variations in simulated MSA<sub>flux</sub> were not different from these in original MSA<sub>flux</sub> even considering the age determination error in the MSA<sub>flux</sub> (Supplementary Figs. 6 and 7).

**Backward trajectory method.** To investigate the source area of MSA contained in ice cores at the SE-Dome, we analyzed air mass position along the backward trajectory from the SE-Dome during the past 7 days using the National Oceanographic and Atmospheric Administration (NOAA) Hybrid Single-Particle Lagrangian Integrated Trajectory (HYSPPLIT) model<sup>40</sup> and National Centers for Environmental Prediction (NCEP) reanalysis data. The initial positions of the air mass were set at 10, 200, 400, 600, 800, and 1000 m above ground level over the SE-Dome site. The initial date and time were every 6 h from 1960 to 2014. We calculated the probability of the existence of an air mass with a 1° resolution. Considering the MSA supply from the ocean surface, we excluded air masses over 1000 m above ground level. Most MSA is deposited on the snow surface by wet deposition<sup>31</sup>. The existence probability was weighted by the daily amount of precipitation when the air mass arrived at the core site. The daily amount of precipitation was extracted from the ERA5 reanalysis dataset<sup>41</sup>. We calculated the cumulative distribution function (CDF) of the existence probability. We described the sea regions where the CDF was 100–60%, 100–40%, and 100–20% as CDF40, CDF60, and CDF80, respectively.

**Satellite-derived chlorophyll-a datasets.** The precursor of DMS in the ocean is dimethylsulfoniopropionate (DMSP), which is produced in phytoplankton. We used the merged multiple satellite Chl-a concentration products provided by the European Space Agency GlobColour project (<http://www.globcolour.info/>) as chlorophyll concentrations for the following discussion. The product is produced by a semianalytical ocean color merging model that estimates Chl-a concentrations, combined dissolved and detrital absorption coefficients, and particle backscattering coefficients from normalized water-leaving radiances retrieved by multiple sensors (SeaWiFS, MERIS, MODIS-Aqua, VIIRS)<sup>42,43</sup>. The temporal coverage and resolution are improved compared to a product of a single sensor<sup>44,45</sup>. The temporal resolution was 8-day and monthly. The spatial resolution was 4 km.

**Frequency of intermediate wind and sea ice conditions.** The DMS emission is promoted when the wind speed is 8–11 m s<sup>-1</sup><sup>9</sup>. The frequency of intermediate wind was defined as the ratio of the total hours when the wind speed at 10 m above sea level was from 8–11 m s<sup>-1</sup> to the total hours of the concerned period, such as season or year. We used the hourly product of the wind speed and sea ice concentration from the ERA5 reanalysis dataset<sup>41</sup>. The spatial resolution was 0.25°. Data were discarded if the sea ice concentration in the grid was greater than 10% because the DMS emission from the ocean to the atmosphere was restricted by sea ice covering on the sea surface.

The sea ice retreat day was defined as the late day when the daily sea ice concentration was less than 10% during April–September in a given year. The daily sea ice concentration was calculated by an hourly sea ice concentration product of ERA5<sup>41</sup>.

The sea ice extent was calculated by multiplying the sea ice concentration by the size of the grid cell. The size of the grid cells was calculated according to the Earth ellipsoid.

**Reporting summary.** Further information on research design is available in the Nature Portfolio Reporting Summary linked to this article.

## Data availability

The data used in this study will be available in Hokkaido University Collection of Scholarly and Academic Papers (HUSCAP) (<http://hdl.handle.net/2115/87441>). The 7-day backward trajectories were calculated by the HYSPLIT model provided by NOAA Air Resources Laboratory (ARL) (<https://www.ready.noaa.gov/>)<sup>40</sup>. The ERA5 data are available on the Copernicus Climate Change Service (C3S) Climate Data Store (<https://cds.climate.copernicus.eu/#/search?text=ERA5&type=dataset>)<sup>41</sup>. The GlobColour data (<http://www.globcolour.info/>) used in this study has been developed, validated, and distributed by ACRI-ST, France<sup>42,43</sup>. The ETOPO1 1 Arc-Minute Global Relief Model is provided by NOAA National Geophysical Data Center (<https://www.ncei.noaa.gov/access/metadata/landing-page/bin/iso?id=gov.noaa.ngdc.mgg.dem:316>)<sup>46</sup>.

## Code availability

The Fortran90 code was used for data analyses. To read NetCDF datasets, we used a netCDF Fortran (version 4.5.4) and a netCDF C (version 4.8.1) libraries developed by UCAR/Unidata (<https://doi.org/10.5065/D6H70CW6>). Additional data analyses were done using the Interactive Data Language (IDL) (version 8.7.1) developed by Exelis Visual Information Solutions, Boulder, Colorado. Map figures were generated using the Generic-Mapping Tools (GMT) (version 6.1.0)<sup>47</sup> (<https://www.generic-mapping-tools.org/>). The statistical tests and graph figures in this study were done using the R software (version 4.1.0)<sup>48</sup> (<https://www.r-project.org/>).

Received: 3 July 2022; Accepted: 13 December 2022;  
Published online: 26 December 2022

## References

- Stefels, J., Steinke, M., Turner, S., Malin, G. & Belviso, S. Environmental constraints on the production and removal of the climatically active gas dimethylsulphide (DMS) and implications for ecosystem modelling. *Biogeochemistry* **83**, 245–275 (2007).
- Charlson, R. J., Lovelock, J. E., Andreae, M. O. & Warren, S. G. Oceanic phytoplankton, atmospheric sulphur, cloud albedo and climate. *Nature* **326**, 655–660 (1987).
- Pandis, S. N., Russell, L. M. & Seinfeld, J. H. The relationship between DMS flux and CCN concentration in remote marine regions. *J. Geophys. Res. Atmos.* **99**, 16945–16957 (1994).
- Simó, R. Production of atmospheric sulfur by oceanic plankton: biogeochemical, ecological and evolutionary links. *Trends Ecol. Evol.* **16**, 287–294 (2001).
- Ridley, J. K., Ringer, M. A. & Sheward, R. M. The transformation of Arctic clouds with warming. *Clim. Change* **139**, 325–337 (2016).
- Mahmood, R., von Salzen, K., Norman, A. L., Galí, M. & Lefebvre, M. Sensitivity of Arctic sulfate aerosol and clouds to changes in future surface seawater dimethylsulfide concentrations. *Atmos. Chem. Phys.* **19**, 6419–6435 (2019).
- Liss, P. S. & Merlivat, L. in *The Role of Air-Sea Interactions in Geochemical Cycling* (ed. Buat-Menard P.) 113–129 (Springer, 1986).
- Huebert, B. J. et al. Linearity of DMS transfer coefficient with both friction velocity and wind speed in the moderate wind speed range. *Geophys. Res. Lett.* **37**, L01605 (2010).
- Bell, T. G. et al. Air-sea dimethylsulfide (DMS) gas transfer in the North Atlantic: Evidence for limited interfacial gas exchange at high wind speed. *Atmos. Chem. Phys.* **13**, 11073–11087 (2013).
- Bell, T. G. et al. Estimation of bubble-mediated air-sea gas exchange from concurrent DMS and CO<sub>2</sub> transfer velocities at intermediate-high wind speeds. *Atmos. Chem. Phys.* **17**, 9019–9033 (2017).
- Galí, M., Lefebvre, M., Devred, E., Simó, R. & Babin, M. Sea-surface dimethylsulfide (DMS) concentration from satellite data at global and regional scales. *Biogeosciences* **15**, 3497–3519 (2018).
- Galí, M., Devred, E., Babin, M. & Lefebvre, M. Decadal increase in Arctic dimethylsulfide emission. *Proc. Natl Acad. Sci. USA* **116**, 19311–19317 (2019).
- Stroeve, J. C. et al. The Arctic's rapidly shrinking sea ice cover: a research synthesis. *Clim. Change* **110**, 1005–1027 (2012).
- AMAP. *Snow, Water, Ice and Permafrost in The Arctic (SWIPA) 2017* (Arctic Monitoring and Assessment Programme (AMAP), Oslo, Norway, 2017).
- Arrigo, K. R. & van Dijken, G. L. Secular trends in Arctic Ocean net primary production. *J. Geophys. Res. Oceans* **116**, C09011 (2011).

16. Bélanger, S., Babin, M. & Tremblay, J.-É. Increasing cloudiness in Arctic dampens the increase in phytoplankton primary production due to sea ice receding. *Biogeosciences* **10**, 4087–4101 (2013).
17. Hayashida, H. et al. Spatiotemporal variability in modeled bottom ice and sea surface dimethylsulfide concentrations and fluxes in the Arctic during 1979–2015. *Global Biogeochem. Cycles* **34**, e2019GB00645 (2020).
18. Sharma, S. et al. Influence of transport and ocean ice extent on biogenic aerosol sulfur in the Arctic atmosphere. *J. Geophys. Res. Atmos.* **117**, D12209 (2012).
19. Pei, Q. et al. Sulfur aerosols in the Arctic, Antarctic, and Tibetan Plateau: current knowledge and future perspectives. *Earth-Sci. Rev.* **220**, 103753 (2021).
20. Oyabu, I. et al. Chemical compositions of solid particles present in the Greenland NEEM ice core over the last 110,000 years. *J. Geophys. Res.* **120**, 9789–9813 (2015).
21. Iizuka, Y. et al. A 60 year record of atmospheric aerosol depositions preserved in a high-accumulation dome ice core, Southeast Greenland. *J. Geophys. Res. Atmos.* **123**, 574–589 (2018).
22. Kuramoto, T. et al. Seasonal variations of snow chemistry at NEEM, Greenland. *Ann. Glaciol.* **52**, 193–200 (2011).
23. Curran, M. A. J. & Jones, G. B. Dimethyl sulfide in the Southern Ocean: seasonality and flux. *J. Geophys. Res. Atmos.* **105**, 20451–20459 (2000).
24. Weller, R. et al. Postdepositional losses of methane sulfonate, nitrate, and chloride at the European Project for Ice Coring in Antarctica deep-drilling site in Dronning Maud Land, Antarctica. *J. Geophys. Res. Atmos.* **109**, D07301 (2004).
25. Iizuka, Y. et al. A firm densification process in the high accumulation dome of Southeastern Greenland. *Arct. Antarct. Alp. Res.* **49**, 13–27 (2017).
26. Furukawa, R. et al. Seasonal-scale dating of a shallow ice core from Greenland using oxygen isotope matching between data and simulation. *J. Geophys. Res. Atmos.* **122**, 10,873–10,887 (2017).
27. Legrand, M. et al. Sulfur-containing species (methanesulfonate and SO<sub>4</sub>) over the last climatic cycle in the Greenland Ice Core Project (central Greenland) ice core. *J. Geophys. Res. Oceans* **102**, 26663–26679 (1997).
28. Maselli, O. J. et al. Sea ice and pollution-modulated changes in Greenland ice core methanesulfonate and bromine. *Clim. Past* **13**, 39–59 (2017).
29. Osman, M. B. et al. Industrial-era decline in subarctic Atlantic productivity. *Nature* **569**, 551–555 (2019).
30. Cole, H. S., Henson, S., Martin, A. P. & Yool, A. Basin-wide mechanisms for spring bloom initiation: how typical is the North Atlantic? *ICES J. Mar. Sci.* **72**, 2029–2040 (2015).
31. Chen, Q., Sherwen, T., Evans, M. & Alexander, B. DMS oxidation and sulfur aerosol formation in the marine troposphere: a focus on reactive halogen and multiphase chemistry. *Atmos. Chem. Phys.* **18**, 13617–13637 (2018).
32. Hayashida, H. et al. Implications of sea-ice biogeochemistry for oceanic production and emissions of dimethyl sulfide in the Arctic. *Biogeosciences* **14**, 3129–3155 (2017).
33. Ardyna, M. et al. Recent Arctic Ocean sea ice loss triggers novel fall phytoplankton blooms. *Geophys. Res. Lett.* **41**, 6207–6212 (2014).
34. Lacour, L. et al. Unexpected winter phytoplankton blooms in the North Atlantic subpolar gyre. *Nat. Geosci.* **10**, 836–839 (2017).
35. Sturm, K., Hoffmann, G., Langmann, B. & Stihler, W. Simulation of  $\delta^{18}\text{O}$  in precipitation by the regional circulation model REMO<sub>iso</sub>. *Hydrol. Process.* **19**, 3425–3444 (2005).
36. Yoshimura, K. Stable water isotopes in climatology, meteorology, and hydrology: a review. *J. Meteorol. Soc. Japan. Ser. II* **93**, 513–533 (2015).
37. Paillard, D., Labeyrie, L. & Yiou, P. Macintosh program performs time-series analysis. *Eos, Transactions American Geophysical Union* **77**, 379–379 (1996).
38. Scholz, D. & Hoffmann, D. L. StalAge—an algorithm designed for construction of speleothem age models. *Quat. Geochronol.* **6**, 369–382 (2011).
39. Iizuka, Y. et al. Glaciological and meteorological observations at the SE-Dome site, southeastern Greenland Ice Sheet. *Bull. Glaciol. Res.* **34**, 1–10 (2016).
40. Stein, A. F. et al. NOAA's hysplit atmospheric transport and dispersion modeling system. *Bull. Am. Meteor. Soc.* **96**, 2059–2077 (2015).
41. Hersbach, H. et al. The ERA5 global reanalysis. *Q. J. R. Meteorol. Soc.* **146**, 1999–2049 (2020).
42. Maritorena, S., Siegel, D. A. & Peterson, A. R. Optimization of a semianalytical ocean color model for global-scale applications. *J. Opt. Soc. Am.* **41**, 2705–2714 (2002).
43. Maritorena, S. & Siegel, D. A. Consistent merging of satellite ocean color data sets using a bio-optical model. *Remote Sens. Environ.* **94**, 429–440 (2005).
44. Maritorena, S., d'Andon, O. H. F., Mangin, A. & Siegel, D. A. Merged satellite ocean color data products using a bio-optical model: Characteristics, benefits and issues. *Remote Sens. Environ.* **114**, 1791–1804 (2010).
45. Zhang, M. et al. Spatiotemporal evolution of the chlorophyll a trend in the North Atlantic Ocean. *Sci. Total Environ.* **612**, 1141–1148 (2018).
46. Amante, C. & Eakins, B. W. ETOPO1 1 Arc-minute global relief model: procedures, data sources and analysis. *NOAA Technical Memorandum NESDIS NGDC-24* (National Geophysical Data Center, NOAA, 2009).
47. Wessel, P. et al. The generic mapping tools version 6. *Geochem. Geophys. Geosyst.* **20**, 5556–5564 (2019).
48. R Core Team. *R: A Language and Environment for Statistical Computing* (R Foundation for Statistical Computing, Vienna, Austria, 2021).

## Acknowledgements

We are grateful to the drilling and initial analysis teams of SE-Dome ice core. The paper was significantly improved as a result of insightful comments by Dr. Hakase Hayashida, Prof. Eric S. Saltzman and an other anonymous reviewer and the handling by two editors Dr. Clare Davis and Dr. Ilka Peeken. This study was supported in part by the Japan Society for the Promotion of Science (JSPS) KAKENHI grant 26257201, 18H05292, and 22J10351: the Arctic Challenge for Sustainability (ArCS II) Project (JPMXD1420318865).

## Author contributions

Y.I. and S.M. designed the study and provided the ice core data. Y.K. and K.F. analyzed the data with the assistance of R.S.. Y.K. and S.M. wrote the manuscript with help of K.F. and Y.I.

## Competing interests

The authors declare no competing interests.

## Additional information

**Supplementary information** The online version contains supplementary material available at <https://doi.org/10.1038/s43247-022-00661-w>.

**Correspondence** and requests for materials should be addressed to Yutaka Kurosaki or Sumito Matoba.

**Peer review information** *Communications Earth & Environment* thanks Hakase Hayashida, Eric S. Saltzman and the other, anonymous, reviewer(s) for their contribution to the peer review of this work. Primary handling editors: Ilka Peeken and Clare Davis. Peer reviewer reports are available.

**Reprints and permission information** is available at <http://www.nature.com/reprints>

**Publisher's note** Springer Nature remains neutral with regard to jurisdictional claims in published maps and institutional affiliations.



**Open Access** This article is licensed under a Creative Commons Attribution 4.0 International License, which permits use, sharing, adaptation, distribution and reproduction in any medium or format, as long as you give appropriate credit to the original author(s) and the source, provide a link to the Creative Commons license, and indicate if changes were made. The images or other third party material in this article are included in the article's Creative Commons license, unless indicated otherwise in a credit line to the material. If material is not included in the article's Creative Commons license and your intended use is not permitted by statutory regulation or exceeds the permitted use, you will need to obtain permission directly from the copyright holder. To view a copy of this license, visit <http://creativecommons.org/licenses/by/4.0/>.

© The Author(s) 2022